High-throughput Screening of Hybrid Quaternary Halide Perovskites for Optoelectronics

Journal:	*Journal of Materials Chemistry A*
Manuscript ID	TA-ART-12-2022-009956.R1
Article Type:	Paper
Date Submitted by the Author:	10-Feb-2023
Complete List of Authors:	Yang, Kesong; University of California, San Diego, NanoEngineering Department Li, Yuheng; University of California, San Diego, NanoEngineering Department Zhang, Jingning; University of California, San Diego, NanoEngineering Department

Journal Name

ARTICLE TYPE

Cite this: DOI: 10.1039/xxxxxxxxxx

Received Date
Accepted Date

DOI: 10.1039/xxxxxxxxxx

www.rsc.org/journalname

High-throughput Screening of Hybrid Quaternary Halide Perovskites for Optoelectronics

Kesong Yang,[*a,b] Yuheng Li,[a] and Jingning Zhang,[a]

Despite their high efficiency and low manufacturing costs, halide perovskite solar cells are suffering from poor stability and lead toxicity, which inhibits their practical use on a large scale. To overcome these challenges, the development of stable and environmentally benign quaternary halide perovskites is a promising solution. Current efforts have mostly focused on inorganic halide double perovskites and are limited to the cubic phase structure. Here we show a high-throughput screening of lead-free hybrid quaternary halide compounds for potential photovoltaic and light-emitting applications. Based on the four different structural templates of inorganic quaternary halide compounds, including but not limited to the traditional cubic double perovskite structure, we have built a comprehensive quantum materials repository containing more than 5,000 hypothetical hybrid quaternary compounds using large-scale *ab-initio* electronic structure calculation. By using automated decomposition enthalpy calculations and other related material descriptors, we have identified eight candidates as promising light absorbers and two candidates as light emitters. All these candidates exhibit robust material stability and desired optoelectronic properties and can be classified into two different crystal systems including the traditional cubic double perovskite phase and the tetragonal phase. This work demonstrates the necessity of considering all the possible quaternary prototype structures in the high-throughput computational materials design.

1 INTRODUCTION

Hybrid organic-inorganic halide perovskites have emerged as one class of most promising light-harvesting materials for next-generation solar cells because of their exceptional properties such as an appropriate band gap, high absorption coefficient, long carrier diffusion length, and high carrier mobility.[1–3] In spite of their high efficiency, the large-scale practical applications of halide perovskites solar cells are hindered by two major challenges including poor stability and lead toxicity.[4–15] To overcome these challenges, novel hybrid materials are being developed with properties that can be superior to or comparable to those of lead halide perovskites. One strategy is to explore hybrid ternary halide compounds including but not limited to traditional perovskite structures. For example, Sn-based organic-inorganic hybrid halide perovskite $MASnI_3$ ($MA=CH_3NH_3$) has been studied for their possible solar-cell applications.[4,7–9] Large-scale computational screening studies were also carried out to search for alternative lead-free hybrid ternary halide compounds.[10,16,17] In our prior work, based on 24 prototype structures including perovskite and non-perovskite structures, we have identified 13 candidates as solar absorbers and 23 candidates as light emitters out of more than 4,500 hypothetical hybrid compounds.[10] It is worth mentioning that non-perovskite structures tend to have larger unit cells and lower symmetry compared to perovskite structures.[18] This inherent low structural dimensionality results in a higher exciton binding energy, even in the absence of organic spacer molecules,[19] which inhibits the separation of photoinduced electron-hole pairs in the solar cells.

Another strategy is to explore the quaternary double perovskite structure. However, most prior experimental studies focused on the preparation and characterization of inorganic double perovskites Cs_2AgBiX_6 (X=Cl or Br).[20–24] The first hybrid double perovskite, $(MA)_2KBiCl_6$ was successfully synthesized in 2016, which shows similar materials properties to the hybrid perovskite $(MA)PbCl_3$.[25] Soon after, halide double perovskite $(MA)_2TlBiBr_6$[26] and $(MA)_2AgBiBr_6$[27] were experimentally synthesized and characterized with a band gap both about 2.0 eV. In comparison with the rapid experimental progress, theoretical and computational studies of hybrid halide double perovskites lag behind. This is mainly due to the complex computational chal-

---

[a] *Department of NanoEngineering and Program of Chemical Engineering, University of California San Diego, 9500 Gilman Drive, Mail Code 0448, La Jolla, California 92093-0448, USA. E-mail: kesong@ucsd.edu*

[b] *Program of Materials Science and Engineering, University of California San Diego, La Jolla, California 92093-0418, USA*

[†] *Electronic supplementary information (ESI) available. See DOI:*

Table 1 Structural properties of the quaternary halide compounds A_2BCX_6 used to extract prototype structures. Original inorganic compound, space group, ICSD number, and Pearson symbol. All the prototype structures are available in the AFLOWLIB and/or Materials Project.

B/C Elements	Stoichiometry	Compounds	Space Group	ICSD Number	Pearson Symbol
B^{1+}/C^{3+}; B^{2+}/C^{2+}	2:1:1:6	$Cs_2AgAuCl_6$	$Fm\bar{3}m$, #225	24516	cF40
		$Cs_2LiInCl_6$	$R\bar{3}m$, #166	65735	hR20
		Cs_2LiGaF_6	$P\bar{3}m1$, #164	202	hP10
		$Cs_2AgAuCl_6$	I4/mmm, #139	26162	tI20

lenges imposed by organic molecules.[28] As a consequence, most prior computational studies were limited to the electronic properties of inorganic double perovskites[29,30] while few were on the hybrid double perovskites.[26,31] Early computational studies concentrated on a limited number of inorganic halide double perovskites containing key elements such as Cu/Ag and Ga/In.[29,30] Asta's team conducted large-scale first-principles calculations for over 1,000 inorganic halide double perovskites in 2019 and identified 11 compounds containing In^+ or Tl^+ elements as promising solar absorbers.[32] Until very recently, Ni *et al.* reported a high-throughput screening of hybrid halide double perovskites and identified three Ag-based candidates for solar cells.[31]

In spite of these encouraging computational efforts, they have all been limited to the cubic double perovskite structure, whereas quaternary halides can have multiple phases. For example, recent work shows that quaternary perovskite oxides have four different phase structures by excluding the layered perovskite structure.[33] Accordingly, one may speculate that candidate materials for promising optoelectronic applications could be missing from prior high-throughput computational studies. In addition, a recent study shows that the use of large organic cations could stabilize $A_2InBiBr_6$ double perovskites,[28] which further highlights the important role of organic cations in the halide double perovskites. So far, there have been no high-throughput screening studies on the complete set of quaternary halide perovskites. Therefore, it is highly worthwhile to explore all the possible quaternary halide compounds beyond the regular cubic double perovskite for searching of alternatives to lead halide perovskites.

In this work, we have carried out a high-throughput computational screening of hybrid quaternary halide compounds for potential optoelectronic applications based on four different structural templates of inorganic quarternary halide compounds using large-scale *ab-initio* electronic structure calculations and automated analysis of material parameters. Eight candidates as solar absorbers and two candidates as light emitters were identified out of more than 5,000 hypothetical hybrid compounds. All these candidates can be categorized into two different crystal systems including the traditional cubic double perovskite phase and tetragonal phase, separately. This work highlights the importance of quaternary halide compounds as an excellent platform for conducting energy materials research beyond photovoltaic solar cells.

2 METHODS

The high-throughput calculations were carried out using the automatic framework AFLOW[34] based on the Vienna *Ab-initio* Simulation Package.[35] The projector augmented wave potentials[36] and generalized gradient approximation (GGA) of the exchange-correlation functional parameterized by Perdew-Burke-Ernzerhof (PBE),[37] were used in the *ab-initio* density functional theory (DFT) calculations. Structures were fully relaxed with a convergence tolerance of 0.01 meV/atom and an automatic *k*-points grid with a separation of 0.05 $Å^{-1}$ for each structure. A denser *k*-points grid with a separation of 0.05 $Å^{-1}$ was used for the static calculations to produce accurate charge density and density of states. The AFLOW code manages other computational settings such as cutoff energy and generates appropriate entries for structural relaxation, static calculations, and electronic band structure calculations sequentially and automatically.[34,38] For the selected final candidate materials, van der Waals (vdW) functional DFT-D3 was used to obtain the accurate equilibrium lattice parameters[39] and hybrid DFT calculations with 25% Hartree-Fock exchange using Heyd-Scuseria-Ernzerhof (HSE) formulation were carried out to predict band gaps.[40]

3 RESULTS AND DISCUSSION

3.1 High-throughput *Ab-initio* Calculations

As the first step, a quantum materials repository that contains hybrid quaternary halide compounds was built using high-throughput *ab-initio* calculations. To do this, we identified all the possible prototype structures based on the inorganic double halide perovskite with a formula of Cs_2BCX_6 (X=F, Cl, Br, and I) from the online quantum materials databases AFLOWLIB.[38] The Cs-contained compounds were selected because Cs cation has a large ionic radius similar to those of organic cations like MA and hybrid compounds are likely to be formed by substituting Cs cations with organic cations. For example, the prototypical inorganic double halide perovskite $A_2BC'X_6$, such as $Cs_2BiAgCl_6$, crystallizes in a face-centered-cubic lattice, with a space group of $Fm\bar{3}m$ (no. 225).[20] The hybrid double halide perovskite can be described as a conventional cell of inorganic double perovskite $A_2BC'X_6$, in which the A-site cation is replaced with the organic cation $(MA)^+$. A total number of 4 unique prototype structures in the formula of Cs_2BCX_6 were identified, see their illustrations of crystal structures in Figure 1. Their complete structural information, including the space group, ICSD number, and Pearson symbol, was listed in Table 1. These prototype structures can be denoted using the unique Pearson symbol. For example, the prototypical double perovskite $Cs_2AgAuCl_6$ with a space group of $Fm\bar{3}m$ and an ICSD number 24516 is denoted with its Pearson symbol of cF40. The other three prototype structures hR20, hP10, and tI20 have rhombohedral, hexagonal, and tetragonal crystal systems, respectively.

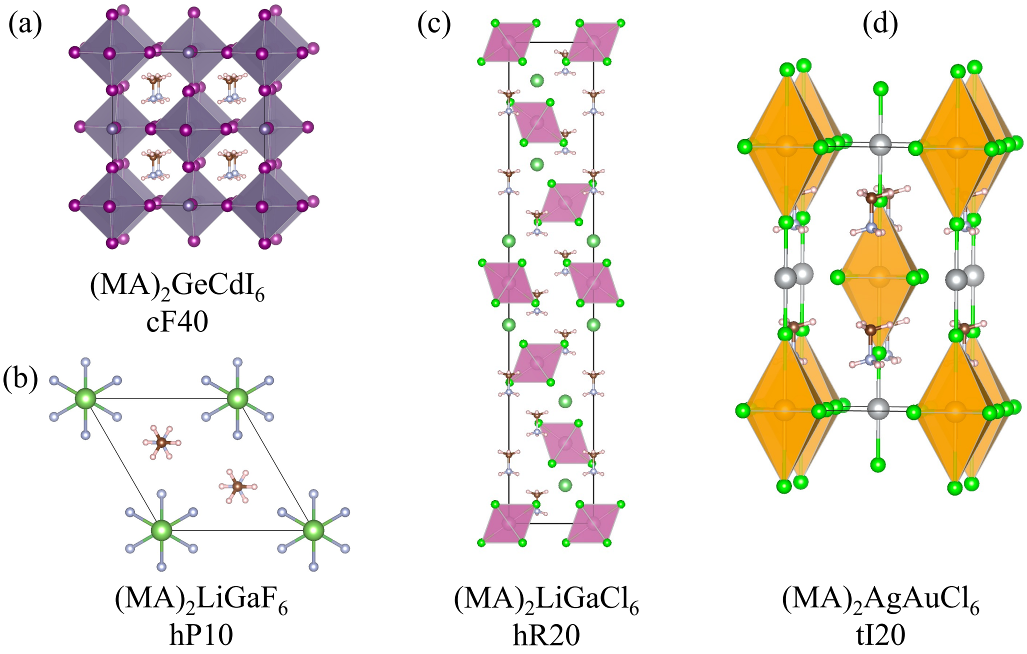

Fig. 1 (Color online) Prototype structure of hybrid quaternary halide compounds (MA)$_2$BC'X$_6$. MA=CH$_3$NH$_3$, B=B$^+$ or B^{2+}, C=C^{3+} or C^{2+}, and X=F$^-$, Cl$^-$, Br$^-$, and I$^-$.

There are two types of formulas for the hybrid quaternary halide perovskites: (MA)$_2$B$^+$C^{3+}X$_6$, and (MA)$_2$B^{2+}C^{2+}X$_6$ (X = F, Cl, Br, and I), in which B could be +1 or +2 cation, and C could be +3 or +2 cation, respectively. The selection of the B and C cations are based on their most common oxidation states. Here, we generated all the possible hybrid quaternary halide compounds by considering all possible element combinations of B and C cations and X anions. A total number of about 5060 hypothetical compounds were obtained for high-throughput *ab-initio* electronic structure calculations.

3.2 High-throughput Screening

There are several common material descriptors for high-throughput screening of optoelectronic materials for photovoltaic and light-emitting applications. These descriptors include thermodynamic stability, band gap, electron (hole) effective masses, *etc.*[10] Next, we discussed the high-throughput screening process based on these material descriptors.

(i) **Decomposition enthalpy (ΔH_d).** The desired compounds with the required properties must be stable and synthesizable. As the first step of the high-throughput screening process, we assessed the thermodynamic stability of all the compounds in the materials repository by analyzing their decomposition enthalpies (ΔH_d). By taking the decomposition pathway A$_2$BCX$_6$ $\rightarrow$ AX + BX$_2$ + ACX$_3$ as one example, the decomposition energy was calculated using the equation: $\Delta H_d = E(AX) + E(BX_2) + E(ACX_3)$ - $E(A_2BCX_6)$, in which $E(AX)$, $E(BX_2)$, $E(ACX_3)$, and $E(A_2BCX_6)$ are the ground-state total energies per unit formula for the compounds AX, BX$_2$, ACX$_3$, and A$_2$BCX$_6$, respectively.

Table 2 summarizes 31 possible decomposition pathways for the quaternary halide compound A$_2$BCX$_6$ by considering all the possible valence states of B/C cations and their competing phases (single-element, binary, and ternary compounds). Note that the decomposition pathway of the compound into component element phases corresponds to the definition of formation enthalpy, which were calculated to ensure the integrity of high-throughput *ab-initio* calculations before the screening process. Accordingly, such a decomposition pathway was not included in the table. Thermodynamic data of these competing phases were collected from our prior computational work on ternary hybrid halide compounds.[10] An in-house software routine was developed to automatically analyze all the possible decomposition pathways and calculate ΔH_d in a high-throughput fashion. To ensure the stability of compounds against their decomposition into competing phases, ΔH_d should be positive for all the possible decomposition pathways. In other words, the lowest ΔH_d selected from all the possible decomposition pathways should be larger than zero. In this step, 784 candidates out of a total number of 5060 compounds were selected by using the initial screening criterion of $\Delta H_d > 0$, which reduces the number of candidate materials by 85%. This indicates that automated decomposition enthalpy calculations are one effective strategy to screen candidate hybrid quaternary halide materials and should be prioritized in the high-throughput materials screening process. This is because such enthalpy calculations only require accurate static total energy calculations for relaxed structures instead of time-consuming electronic band structure calculations that usually involves hundreds of *k*-points along the high-symmetry paths in reciprocal space, particularly for the quaternary halide materials that usually have large unit cells.

(ii) Band gap (E_g). A light-absorbing material for solar cells can have either a direct band gap or an indirect band gap. In

Table 2 Summary of possible decomposition pathways used to calculate the decomposition enthalpy (per formula unit) for the quaternary halide A_2BCX_6 compounds.

No.	Pathway
1	$AX + BX_2 + ACX_3 - A_2BCX_6$
2	$AX + CX_2 + ABX_3 - A_2BCX_6$
3	$AX + ABX_2 + CX_3 - A_2BCX_6$
4	$AX + ACX_2 + BX_3 - A_2BCX_6$
5	$2*AX + BX + CX_3 - A_2BCX_6$
6	$2*AX + CX + BX_3 - A_2BCX_6$
7	$2*AX + BX_2 + CX_2 - A_2BCX_6$
8	$BX_2 + A_2CX_4 - A_2BCX_6$
9	$A_2BX_4 + CX_2 - A_2BCX_6$
10	$CX_3 + A_2BX_3 - A_2BCX_6$
11	$BX_3 + A_2CX_3 - A_2BCX_6$
12	$(AX + 2*BX + A_3C_2X_9 - 2*A_2BCX_6)/2$
13	$(AX + 2*CX + A_3B_2X_9 - 2*A_2BCX_6)/2$
14	$(3*AX + 2*CX_2 + AB_2X_5 - 2*A_2BCX_6)/2$
15	$(3*AX + 2*BX_2 + AC_2X_5 - 2*A_2BCX_6)/2$
16	$(BX + ABX_2 + A_3C_2X_9 - 2*A_2BCX_6)/2$
17	$(CX + ACX_2 + A_3B_2X_9 - 2*A_2BCX_6)/2$
18	$(4*AX + 3*BX_2 + A_2C3X_8 - 3*A_2BCX_6)/3$
19	$(4*AX + A_2B3X_8 + 3*CX_2 - 3*A_2BCX_6)/3$
20	$(6*AX + 3*BX_3 + CX_3 + 2*C - 3*A_2BCX_6)/3$
21	$(6*AX + 3*CX_3 + BX_3 + 2*B - 3*A_2BCX_6)/3$
22	$(3*AX + 3*CX + 2*BX_3 + A_3BX_6 - 3*A_2BCX_6)/3$
23	$(3*AX + 3*BX + 2*CX_3 + A_3CX_6 - 3*A_2BCX_6)/3$
24	$(3*BX + A_2BX_3 + 2*A_3C_2X_9 - 4*A_2BCX_6)/4$
25	$(3*CX + A_2CX_3 + 2*A_3B_2X_9 - 4*A_2BCX_6)/4$
26	$(3*A_3B_2X_9 + 4*C + A_3C_2X_9 - 6*A_2BCX_6)/6$
27	$(3*A_3C_2X_9 + 4*B + A_3B_2X_9 - 6*A_2BCX_6)/6$
28	$(9*AX + A_3C_2X_9 + 6*BX_3 + 4*C - 6*A_2BCX_6)/6$
29	$(9*AX + A_3B_2X_9 + 6*CX_3 + 4*B - 6*A_2BCX_6)/6$
30	$(3*A_3B_2X_9 + 3*AX + 2*CX_3 + 4*C - 6*A_2BCX_6)/6$
31	$(3*A_3C_2X_9 + 3*AX + 2*BX_3 + 4*B - 6*A_2BCX_6)/6$

general, the band gap energy should be in the range from 0.8 to 2.2 eV, which is selected according to the relationship between the Shockley-Queisser efficiency limit and band gap energy.[41] For visible-light emitting applications, the band gap of candidate materials is generally in the range of 1.65 to 3.0 eV, which partially overlaps with the photovoltaic materials. To search for promising materials for a broad spectrum of optoelectronic applications, all the candidate materials with band gaps in the range of 0.8 to 3.0 eV should be considered. In addition, it is well-known that standard DFT calculations generally underestimate the band gap (E_g^{GGA}) of semiconductors and insulators by 30%-40%.[42,43] Therefore, we could narrow the search space of candidate materials by defining the band-gap range of $0.5 < E_g^{GGA} < 2.3$ eV, which returns us 239 entries out of 784 compounds by reducing search space of the candidate materials by 70%. As shown later, more accurate band gaps (E_g^{HSE}) of the selected final candidates will be calculated using hybrid functional.

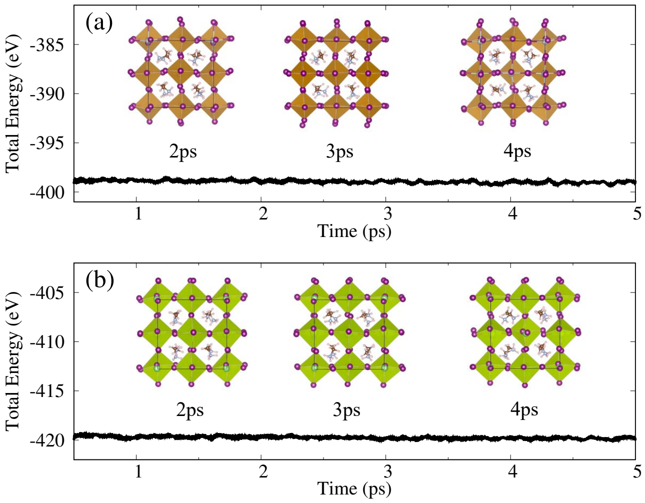

Fig. 2 (Color online) Total energy during 5 ps *ab-initio* molecular dynamics (AIMD) simulations at 300K for two selected candidate materials: (a) $(MA)_2AgAuI_6$ and (b) $(MA)_2GaCeI_6$.

(iii) Electron and hole effective masses (m_e^* and m_h^*). A key factor determining the photovoltaic efficiency of a solar cell is an efficient charge-carrier separation in the light absorber, which requires fast charge transport.[3] The transport of charge carrier in a semiconductor is closely related to the carrier mobility μ_e (μ_h) that can be linked to the electron (and hole) effective mass m_e^* (m_h^*) by using the equation: $\mu_e = e < \tau > /m_e^*$ ($\mu_h = e < \tau > /m_h^*$), in which e is the fundamental charge and $< \tau >$ is the average scattering time, and m_e^* (m_h^*) is electron (hole) effective mass.[44] Consequently, the smaller the electron (hole) effective mass is, the higher the electron (hole) mobility is, and the faster the carrier transport is. Hence, electron effective mass (m_e^*) and hole effective mass (m_h^*) can be used as another group of material descriptors. m_e^* is directly related to the curvature of the bottom conduction bands near the conduction band minimum (CBM) and m_h^* the curvature of the top valence bands near the valence band maximum (VBM) of a solid-state material. It is worth mentioning that, in spite of the underestimation of the band gaps from standard DFT-GGA calculations, the shape of electronic band structures at GGA level is rather reliable and resembles the experiment well.[45] This conclusion enables us to use m_e^* and m_h^* directly produced from standard DFT-GGA calculations as new materials descriptors, and more details can be found from our prior work.[10] In this work, we set a common upper limit of 1.5 m_0 as the screening criterion, *i.e.*, $m_e^* \leq 1.50\ m_0$ and $m_h^* \leq 1.5\ m_0$, where m_0 is free electron rest mass. This screening process narrows down the number of candidate compounds to 94 from 239 entries.

(iv) Compounds with toxic B-site and C-site elements including Hg, Cd, Pb, and Tl were removed. In addition, the Sn(Ge)-based quaternary halide perovskites were also excluded from our final list since they can be considered as the derivatives of well-studied Sn(Ge)-based ternary compounds. This step further reduces the number of candidate compounds to 54 entries. As the hybrid counterpart of the well-studied inorganic double

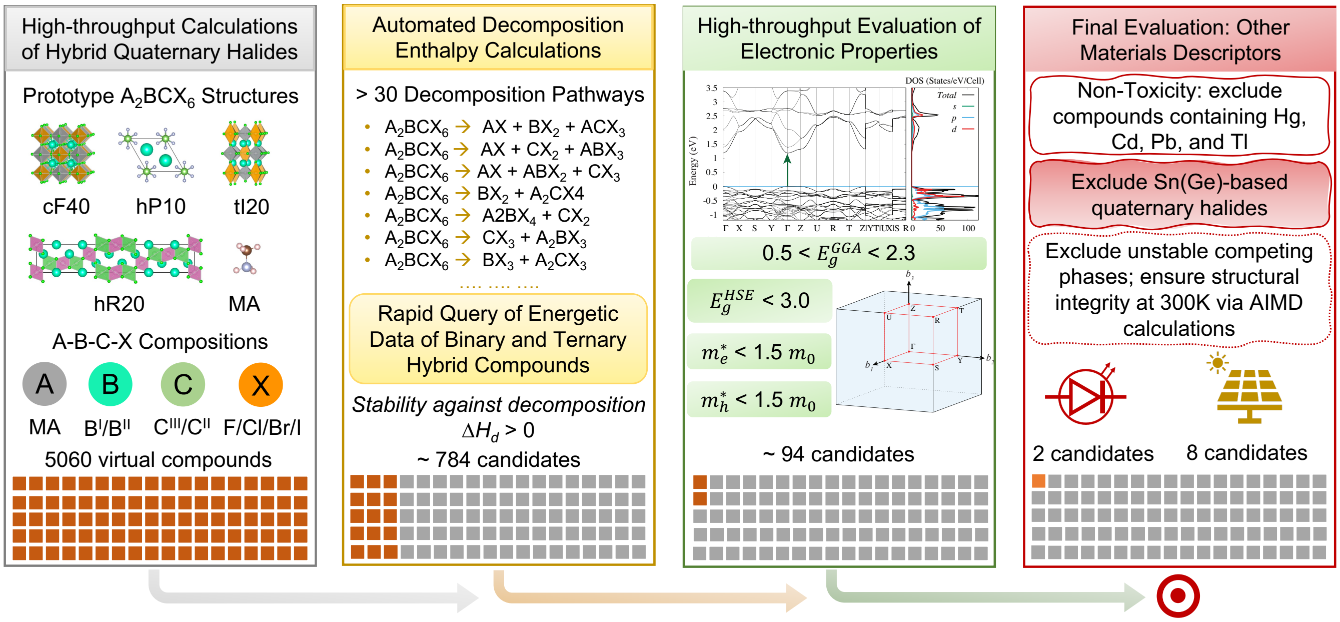

Fig. 3 (Color online) Schematic illustration of the high-throughput screening flowchart. A total number of about 5060 virtual compounds were generated from the four types of prototype A_2BCX_6 structures using various combinations of (B^+, C^{3+}) and (B^{2+}, C^{2+}) and organic MA cation. Automated decomposition enthalpy calculations were performed to screen stable compounds via a rapid query of energetic data of binary and ternary hybrid compounds over more than 30 possible decomposition pathways. Electronic properties including electronic band structure and electron (hole) effective masses were evaluated in a high-throughput fashion. The final candidates were selected by excluding the compounds containing toxic elements and Sn(Ge) elements and the compounds that cannot maintain structural integrity at room temperature.

perovskites $Cs_2AgBiBr_6$,[23,46] experimentally synthesized hybrid double perovskites $(MA)_2AgBiBr_6$ and $(MA)_2AgBiI_6$ were also excluded from our final list.[27,47]

(v) Formation enthalpy difference (ΔH_f^{diff}). As shown in **Figure 1**, one stochiometry of the quaternary halide double perovskite has four types of phases, suggesting that there might exist competing phases for the given composition. To select the most synthesizable compounds, here we define ΔH_f^{diff} as the calculated formation enthalpy difference between each phase and its energetically most favorable competing phase of the same composition. If the ΔH_f^{diff} is less than room-temperature thermal energy (about 26 meV), then the two phases were considered as both synthesizable; otherwise, the phase with the lower formation enthalpy is selected. This screening process returns a total number of 27 entries.

(vi) Room-temperature structural integrity. To ensure room-temperature structural stability of candidate materials, we further carried out *ab-initio* molecular dynamics (AIMD) calculations at 300 K. The entire molecular dynamics simulation lasted 5 ps with a time step of 1 fs using the Nos*é*-Hoover method. **Figure 2** shows the calculated total energy as a function of AIMD simulation time for two selected candidate compounds $(MA)_2AgAuI_6$ and $(MA)_2GaCeI_6$. During the simulation period of 5 ps, if the total energy of a candidate compound oscillates within a fairly narrow energy range and the selected geometrical structures at 2, 3, and 4 ps all exhibit an ordered crystalline phase, then it means that the room-temperature structural integrity can be maintained and the candidate materials are stable. Otherwise, the candidate materials will be eliminated from the final list.

The above screening procedure is summarized in Figure 3, which leads to a total number of 10 candidate compounds for potential optoelectronic applications. To correct the underestimated band gaps from the standard DFT calculations, we further carried out hybrid functional theory calculations for these 10 candidate compounds within HSE formalism,[40] which can yield reliable band gaps close to experimental values.[48] Based on the corrected band gaps, 8 candidate compounds with corrected band gaps in the range between 0.9 and 1.6 eV are proposed for promising photovoltaic applications and 2 candidate compounds with corrected band gaps larger than 2.5 eV, *i.e.*, $(MA)_2GaCeI_6$ and $(MA)_2GaNdI_6$, are proposed for light-emitting applications, see their relaxed structure files on GitHub.[49]

3.3 Discussion

In this section, we discuss the crystal structure, composition, and electronic structures of the selected compounds. The calculated properties of all the 10 candidate compounds are summarized in Table 3. They are classified into three categories based on their composition and lattice type, including Ag-, Cu-, and Ga(In)-based compounds. Figure 4a-d and 4a'-d' show the calculated electronic band structure and partial density of states (PDOS) of the four representative candidates, $(MA)_2AgAuI_6$, $(MA)_2CuAuI_6$, $(MA)_2InBiBr_6$, and $(MA)_2GaCeI_6$, respectively. Note that the incorporation of the organic MA cation can cause the structural distortion of the lattice, and the lattice symmetry could be downgraded as orthorhombic from the original face-centered cubic (cF40) and tetragonal (tI20) lattice. Hence, a *k*-path generated from simple orthorhombic lattice (ORC) was used in our electronic band structure calculations.[50]

Table 3 Properties of selected hybrid quaternary halide materials: compound, Pearson symbol of the prototype structures, equilibrium lattice parameters, calculated band gaps (in eV) from GGA-PBE (E_g^{GGA}) and HSE (E_g^{HSE}) approaches, band-gap type [Direct (D) or Indirect (I)], k-path from VBM to CBM, and electron (hole) effective mass m_e^* (m_h^*) near the CBM (VBM) (in m_0). If a VBM is between two k-points such as Γ and Z, then the VBM is labeled as (Γ, Z), and decomposition enthalpy (ΔH_d in eV per f.u.). * indicates that the Cs-based inorganic counterpart of the predicted hybrid materials have been experimentally synthesized.

Compound	Pearson	Lattice Parameters			E_g^{GGA}	E_g^{HSE}	Band-gap	k_{VBM} →	m_e^*	m_h^*	ΔH_d
	Symbol	a	b	c			Type	k_{CBM}			
$(MA)_2AgAuF_6$	tI20	6.153	6.182	10.105	0.69	1.38	(I)	(Γ,Y)-Y	0.38	0.42	0.33
$(MA)_2AgAuCl_6{}^*$	cF40	10.192	11.544	10.818	0.78	1.41	(I)	(Z,U)-U	0.18	0.31	0.53
$(MA)_2AgAuBr_6{}^*$	cF40	10.774	11.897	11.175	0.63	1.19	(I)	(Z,U)-U	0.18	0.45	0.55
$(MA)_2AgAuI_6$	cF40	12.306	11.658	11.989	0.65	1.13	(I)	Γ-R	0.21	0.40	0.49
$(MA)_2CuAuCl_6$	tI20	7.230	7.279	11.762	0.52	0.93	(I)	(Γ,Y)-X	0.16	0.14	0.12
$(MA)_2CuAuBr_6$	tI20	7.566	7.639	12.003	0.50	0.92	(I)	(Γ,Y)-X	0.14	0.12	0.15
$(MA)_2CuAuI_6$	tI20	8.152	8.211	12.480	0.64	1.07	(I)	(Γ,Y)-X	0.18	0.14	0.74
$(MA)_2InBiBr_6$	cF40	11.816	11.766	11.788	0.74	1.13	(D)	Γ-Γ	0.66	0.10	0.13
$(MA)_2GaCeI_6$	cF40	12.509	12.469	12.493	2.13	2.75	(I)	R-Γ	0.72	0.31	0.65
$(MA)_2GaNdI_6$	cF40	12.455	12.412	12.411	2.22	2.92	(I)	R-Γ	0.72	0.32	0.62

$(MA)_2AgAuI_6$, representative of the cF40 candidates containing Ag^+ and Au^{3+} cations, has an indirect band gap of 1.13 eV with VBM at Γ (or X) and CBM at R point, see Figure 4a. The calculated PDOS shows that the conduction band (CB) mainly consists of I 5p orbitals and a small portion of Au 5d orbitals while Ag 4d orbitals nearly have no contribution to the CB, suggesting oxidation states of Ag^+ and Au^{3+} (Figure 4a'). In contrast, the valence band (VB) is mainly contributed to I 5p orbitals. The I 5p and Au 5d orbital contributions lead to dispersive bands near the VBM and CBM, yielding small m_h^* and m_e^*. Other predicted materials in the same category include $(MA)_2AgAuBr_6$, $(MA)_2AgAuCl_6$, and $(MA)_2AgAuF_6$. Interestingly, a very recent computational screening study of lead-free hybrid halide double perovskites also predicted that the compounds $(MA)_2AgAuBr_6$ and $(MA)_2AgAuCl_6$ are promising for perovskite solar cells.[31] An earlier computational study by Nakajima *et al.* predicted candidate hybrid double halide perovskites $(MA)_2AgAuBr_6$ and $(FA)_2AgAuI_6$.[51] However, it is worth that the compound $(MA)_2AgAuF_6$ exhibits a ground-state tI20 lattice structure rather than the cF40 structure, unlike the other three Ag-based cF40 compounds. This may explain why these prior computational studies did not report $(MA)_2AgAuF_6$. Although the experimental synthesis of the hybrid materials based on the inorganic counterparts of this category of compounds has not been reported yet, the pure inorganic compounds $Cs_2AgAuCl_6$ and $Cs_2AgAuBr_6$ have been synthesized in prior experiments.[52,53]

$(MA)_2CuAuI_6$, one example of tI20 candidates containing Cu^+ and Au^{3+} cations, shows an indirect-like band gap of 1.07 eV with VBM at the reciprocal point between Γ and Y and and CBM at X point (Figure 4b). However, a direct electron excitation at U point is expected to be dominant due to the extremely small difference between the VBM and the highest occupied energy level at U point as well as the CBM and the lowest unoccupied energy level at U point. From this perspective, this class of compounds can also be considered as direct. Similar to the case of Ag-based cF40 compounds, the calculated PDOS shows that Cu exists as Cu^+ cation and Au exists as Au^{3+} cation (Figure 4b'), and the I 5p and Au 5d orbitals are responsible for the low m_h^* and m_e^*. A prior computational study reported the discovery of $(MA)_2CuAuBr_6$ and $(MA)_2CuAuI_6$ in a cubic double perovskite structure (*i.e.*, cF40 structure) as candidate photovoltaic materials.[51] However, our calculations show that their tI20 structure in a tetragonal phase is energetically more favorable than their cubic phase by around 161 and 241 meV per formula unit, respectively, which awaits further experimental verification.

$(MA)_2InBiBr_6$, belonging to cF40 structure like Ag-based compounds, has a direct band gap of 1.13 eV with VBM and CBM at Γ point, as shown in Figure 4c. The calculated PDOS of the In cation shows its 5p orbitals are all unoccupied while 5s orbitals are almost fully occupied (Figure 4c'), suggesting that In exists as In^+ with an electron configuration of $5s^2 5p^0$. In contrast, a large portion of Bi 6p orbitals contribute to the VB of the compound and are thus unoccupied, implying its Bi^{+3} oxidation state. Interestingly, note that the VBM is mainly composed of In 5s orbitals instead of Br 4p orbitals, which explains why this compound has relatively low m_h^*. Note that the pure inorganic double perovskite $Cs_2InBiCl_6$ has been proposed to be a promising photovoltaic absorber theoretically mainly because of its small band gap and small electron and hole effective masses.[30] However, its extremely small decomposition enthalpy, about 1 meV/atom, implies that this compound is not thermodynamically stable enough against decomposition.[24,28,54] In fact, Xiao *et al.* have carried out an attempted solid-state synthesis of $Cs_2InBiCl_6$ but did not find desired double perovskite structure and concluded that the In(I)-based double perovskites are unstable against oxidation into In(III)-based compounds.[54] Nevertheless, Volonakis *et al.* found that the In(I)-based $AInBiX_6$ double perovskites become progressively more stable as the A-site cation changes from K to Cs from DFT calculations.[28] On the basis of this trend and extrapolation of the curve of decomposition enthalpy versus the ionic radius of the A-site cation, they proposed that the In-based hybrid perovskite,

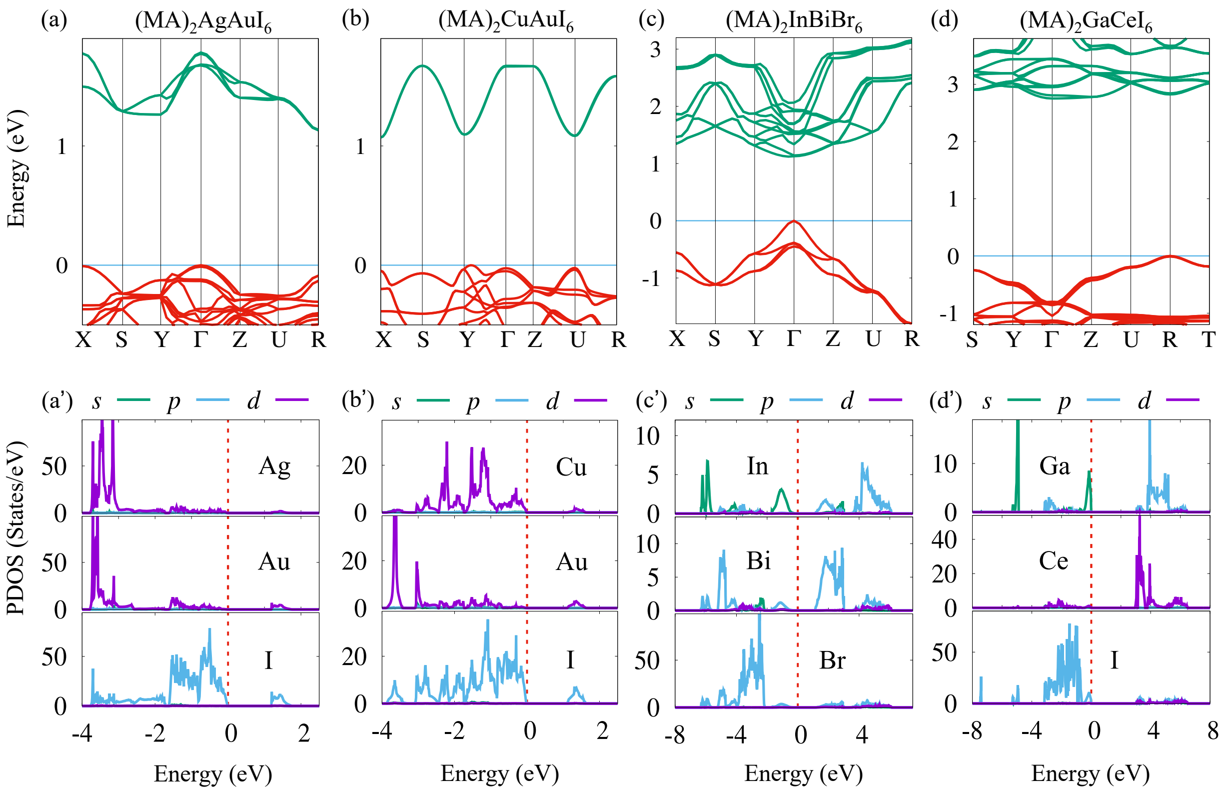

Fig. 4 (Color online) Calculated electronic band structure and partial density of states (PDOS) with HSE06 correction for the representative candidates: (a) $(MA)_2AgAuI_6$, (b) $(MA)_2CuAuI_6$, (c) $(MA)_2InBiBr_6$, and $(MA)_2GaCeI_6$. The Fermi level is indicated by the straight line at 0.

$A_2InBiBr_6$, could be stabilized by using large organic MA cation, although the accurate decomposition enthalpy from DFT calculations was not obtained due to the great computational challenges imposed by the organic cations.[28] Interestingly, our calculations show that the hybrid perovskite $(MA)_2InBiBr_6$ has large decomposition enthalpy of around 130 meV per formula unit, implying robust thermodynamic stability. Its two similar compounds $(MA)_2InBiCl_6$ and $(MA)_2InBiI_6$ were not selected because of the following reasons. $(MA)_2InBiCl_6$ has a negative decomposition enthalpy of -20 meV per formula unit via a spontaneous decomposition into In(III)-based compound $(MA)_3In_2Cl_9$ and other products. $(MA)_2InBiI_6$ cannot maintain its structural integrity due to the large changes of total energy as indicated from our AIMD calculations, although it was proposed to be a candidate photovoltaic absorber in an early study.[51]

$(MA)_2GaCeI_6$, representing the two cF40 candidates containing rare-earth elements, shows an indirect band gap of 2.75 eV with VBM at R point and CBM at Γ point, see Figure 4d. The PDOS shows that Ga 4*p* orbitals are almost fully unoccupied while Ga 4*s* orbitals are fully occupied, indicating that Ga exists as Ga^+ cation with an electron configuration of $4s^2 4p^0$, as shown in Figure 4d'. In contrast, most of Ce 5*d* orbitals are unoccupied, indicating that Ce exists as Ce^{+3} cations with an electron configuration of $5d^0 6s^0$. Moreover, the VBM consists primarily of Ga 4*s* orbitals while CBM mainly consists of Ce 5*d* orbitals, resulting in low m_h^* and m_e^*. Similar electronic properties also appear in the compound $(MA)_2GaNdI_6$, which make them promising candidates as light emitters, thus being worthy of further experimental validation. It is noted that several other Ga-based hybrid compounds including $(MA)_2GaBiBr_6$ $(MA)_2GaBiI_6$ have been suggested as candidate light absorbers because of their ideal bandgaps.[51] However, these two compounds are not selected in our final list because $(MA)_2GaBiBr_6$ has a negative decomposition enthalpy of about -55 meV and will be decomposed into $(MA)_3Ga_2Br_9$ spontaneously while $(MA)_2GaBiI_6$ has a positive decomposition enthalpy but it cannot maintain room-temperature structural integrity.

Summary

In summary, we have demonstrated a successful application of the high-throughput computational screening approach in the accelerated discovery of novel hybrid quaternary halide perovskites for optoelectronic applications. By using large-scale *ab-initio* calculations, we have generated a quantum materials repository containing more than 5,000 hypothetical hybrid materials based on the four different structural templates of inorganic quaternary halide compounds. Upon using automated analysis of decomposition enthalpy and other material descriptors, we identified eight candidates for photovoltaic cells, including $(MA)_2AgAuX_6$ (X=F, Cl, Br, and I), $(MA)_2CuAuX_6$ (X=Cl, Br, and I), and $(MA)_2InBiBr_6$, and two candidates for light-emitting applications including $(MA)_2GaCeI_6$ and $(MA)_2GaNdI_6$. All these candidates were found in the two different crystal systems. This work shows an effective strategy to search for novel lead-free hybrid quaternary halide compounds for optoelectronic applications and it is essential to consider a full set of quaternary prototype structures in the high-throughput materials design.

Acknowledgments

This work used Expanse cluster at San Diego Supercomputer Center through allocation DMR160045 from the Extreme Science and Engineering Discovery Environment (XSEDE), which was supported by National Science Foundation grant number #1548562. The authors thank Jianli Cheng and Sicong Jiang for useful comments.

References

1 A. Kojima, K. Teshima, Y. Shirai and T. Miyasaka, *J. Am. Chem. Soc.*, 2009, **131**, 6050–6051.
2 G. Hodes, *Science*, 2013, **342**, 317–318.
3 T. M. Brenner, D. A. Egger, L. Kronik, G. Hodes and D. Cahen, *Nat. Rev. Mater.*, 2016, **1**, 15007.
4 F. Hao, C. C. Stoumpos, D. H. Cao, R. P. H. Chang and M. G. Kanatzidis, *Nat. Photon.*, 2014, **8**, 489–494.
5 J. H. Kim, S. T. Williams, N. Cho, C.-C. Chueh and A. K.-Y. Jen, *Adv. Energy Mater.*, 2015, **5**, 1401229.
6 A. Polman, M. Knight, E. C. Garnett, B. Ehrler and W. C. Sinke, *Science*, 2016, **352**, aad4424.
7 N. K. Noel, S. D. Stranks, A. Abate, C. Wehrenfennig, S. Guarnera, A.-A. Haghighirad, A. Sadhanala, G. E. Eperon, S. K. Pathak, M. B. Johnston, A. Petrozza, L. M. Herz and H. J. Snaith, *Energy Environ. Sci.*, 2014, **7**, 3061–3068.
8 M. H. Kumar, S. Dharani, W. L. Leong, P. P. Boix, R. R. Prabhakar, T. Baikie, C. Shi, H. Ding, R. Ramesh, M. Asta, M. Graetzel, S. G. Mhaisalkar and N. Mathews, *Adv. Mater.*, 2014, **26**, 7122–7127.
9 C. Bernal and K. Yang, *J. Phys. Chem. C*, 2014, **118**, 24383–24388.
10 Y. Li and K. Yang, *Energy Environ. Sci.*, 2019, **12**, 2233–2243.
11 Y. Chen, Y. Lei, Y. Li, Y. Yu, J. Cai, M.-H. Chiu, R. Rao, Y. Gu, C. Wang, W. Choi, H. Hu, C. Wang, Y. Li, J. Song, J. Zhang, B. Qi, M. Lin, Z. Zhang, A. E. Islam, B. Maruyama, S. Dayeh, L.-J. Li, K. Yang, Y.-H. Lo and S. Xu, *Nature*, 2020, **577**, 209.
12 Y. Lei, Y. Chen, R. Zhang, Y. Li, Q. Yan, S. Lee, Y. Yu, H. Tsai, W. Choi, K. Wang, Y. Luo, Y. Gu, X. Zheng, C. Wang, C. Wang, H. Hu, Y. Li, B. Qi, M. Lin, Z. Zhang, S. A. Dayeh, M. Pharr, D. P. Fenning, Y.-H. Lo, J. Luo, K. Yang, J. Yoo, W. Nie and S. Xu, *Nature*, 2020, **583**, 790.
13 Y. Li and K. Yang, *WIREs Comput Mol Sci.*, 2021, **11**, e1500.
14 J. Wong and K. Yang, *Sol. RRL*, 2021, **5**, 2000395.
15 Y. Lei, Y. Li, C. Lu, Q. Yan, Y. Wu, F. Babbe, H. Gong, S. Zhang, J. Zhou, R. Wang, R. Zhang, Y. Chen, H. Tsai, Y. Gu, H. Hu, Y.-H. Lo, W. Nie, T. Lee, J. Luo, K. Yang, K.-I. Jang and S. Xu, *Nature*, 2022, **608**, 317.
16 D. Yang, J. Lv, X. Zhao, Q. Xu, Y. Fu, Y. Zhan, A. Zunger and L. Zhang, *Chem. Mater.*, 2017, **29**, 524–538.
17 S. Lu, Q. Zhou, Y. Ouyang, Y. Guo, Q. Li and J. Wang, *Nat. Commun.*, 2018, **9**, 3405.
18 F. Massuyeau, T. Broux, F. Coulet, A. Demessence, A. Mesbah and R. Gautier, *Adv. Mater.*, 2022, **34**, 2203879.
19 Y. Nah, D. Solanki and D. H. Kim, *Cell Rep. Phys. Sci.*, 2022, **3**, 101171.
20 G. Volonakis, M. R. Filip, A. A. Haghighirad, N. Sakai, B. Wenger, H. J. Snaith and F. Giustino, *J. Phys. Chem. Lett.*, 2016, **7**, 1254–1259.
21 A. H. Slavney, T. Hu, A. M. Lindenberg and H. I. Karunadasa, *J. Am. Chem. Soc.*, 2016, **138**, 2138–2141.
22 M. R. Filip, S. Hillman, A. A. Haghighirad, H. J. Snaith and F. Giustino, *J. Phys. Chem. Lett.*, 2016, **7**, 2579–2585.
23 E. T. McClure, M. R. Ball, W. Windl and P. M. Woodward, *Chem. Mater.*, 2016, **28**, 1348–1354.
24 C. N. Savory, A. Walsh and D. O. Scanlon, *ACS energy letters*, 2016, **1**, 949–955.
25 F. Wei, Z. Deng, S. Sun, F. Xie, G. Kieslich, D. M. Evans, M. A. Carpenter, P. D. Bristowe and A. K. Cheetham, *Mater. Horiz.*, 2016, **3**, 328–332.
26 Z. Deng, F. Wei, S. Sun, G. Kieslich, A. K. Cheetham and P. D. Bristowe, *J. Mater. Chem. B*, 2016, **4**, 12025–12029.
27 F. Wei, Z. Deng, S. Sun, F. Zhang, D. M. Evans, G. Kieslich, S. Tominaka, M. A. Carpenter, J. Zhang, P. D. Bristowe *et al.*, *Chem. Mater.*, 2017, **29**, 1089–1094.
28 G. Volonakis, A. A. Haghighirad, H. J. Snaith and F. Giustino, *J. Phys. Chem. Lett.*, 2017, **8**, 3917–3924.
29 X.-G. Zhao, D. Yang, Y. Sun, T. Li, L. Zhang, L. Yu and A. Zunger, *J. Am. Chem. Soc.*, 2017, **139**, 6718–6725.
30 X.-G. Zhao, J.-H. Yang, Y. Fu, D. Yang, Q. Xu, L. Yu, S.-H. Wei and L. Zhang, *J. Am. Chem. Soc.*, 2017, **139**, 2630–2638.
31 X. Ni, Y. Liu, Y. Ji, C. Hu and Y. Li, 2022, **10**, 16822–16827.
32 Y. Cai, W. Xie, Y. T. Teng, P. C. Harikesh, B. Ghosh, P. Huck, K. A. Persson, N. Mathews, S. G. Mhaisalkar, M. Sherburne and M. Asta, *Chem. Mater.*, 2019, **31**, 5392–5401.
33 M. Askerka, Z. Li, M. Lempen, Y. Liu, A. Johnston, M. I. Saidaminov, Z. Zajacz and E. H. Sargent, *J. Am. Chem. Soc.*, 2019, **141**, 3682–3690.
34 S. Curtarolo, W. Setyawan, G. L. W. Hart, M. Jahnatek, R. V. Chepulskii, R. H. Taylor, S. Wang, J. Xue, K. Yang, O. Levy, M. Mehl, H. T. Stokes, D. O. Demchenko, and D. Morgan, *Comput. Mater. Sci.*, 2012, **58**, 218–226.
35 G. Kresse and J. Furthmüller, *Phys. Rev. B*, 1996, **54**, 11169–11186.
36 G. Kresse and D. Joubert, *Phys. Rev. B*, 1999, **59**, 1758–1775.
37 J. P. Perdew, K. Burke and M. Ernzerhof, *Phys. Rev. Lett.*, 1996, **77**, 3865–3868.
38 S. Curtarolo, W. Setyawan, S. Wang, J. Xue, K. Yang, R. H. Taylor, L. J. Nelson, G. L. W. Hart, S. Sanvito, M. B. Nardelli, N. Mingo and O. Levy, *Comput. Mater. Sci.*, 2012, **58**, 227–235.
39 S. Grimme, J. Antony, S. Ehrlich and H. Krieg, *J. Chem. Phys.*, 2010, **132**, 154104.
40 J. Heyd, G. E. Scuseria and M. Ernzerhof, *J. Chem. Phys.*, 2003, **118**, 8207–8215.
41 W. Shockley and H. J. Queisser, *J. Appl. Phys.*, 1961, **32**, 510–519.

42 J. P. Perdew and M. Levy, *Phys. Rev. Lett.*, 1983, **51**, 1884–1887.

43 F. Bechstedt and R. Del Sole, *Phys. Rev. B*, 1988, **38**, 7710–7716.

44 Y. Peter and M. Cardona, *Fundamentals of Semiconductors: Physics and Materials Properties*, Springer Science & Business Media, 2010.

45 M. Jain, J. R. Chelikowsky and S. G. Louie, *Phys. Rev. Lett.*, 2011, **107**, 216806.

46 W. Pan, H. Wu, J. Luo, Z. Deng, C. Ge, C. Chen, X. Jiang, W.-J. Yin, G. Niu, L. Zhu, L. Yin, Y. Zhou, Q. Xie, X. Ke, M. Sui and J. Tang, *Nat. Photon.*, 2017, **11**, 726.

47 M. S. Shadabroo, H. Abdizadeh and M. R. Golobostanfard, *Mater. Sci. Semicond. Process.*, 2021, **125**, 105639.

48 A. J. Garza and G. E. Scuseria, *J. Phys. Chem. Lett.*, 2016, **7**, 4165–4170.

49 `https://github.com/ksyang2013/hybrid_quaternary_halides`.

50 W. Setyawan and S. Curtarolo, *Comput. Mater. Sci.*, 2010, **49**, 299–312.

51 T. Nakajima and K. Sawada, *J. Phys. Chem. Lett.*, 2017, **8**, 4826–4831.

52 N. Elliott, *J. Chem. Phys.*, 1934, **2**, 419–420.

53 P. Gütlich, B. Lehnis and J. Strähle, *Zeitschrift für Naturforschung B*, 1982, **37**, 550–556.

54 Z. Xiao, K.-Z. Du, W. Meng, J. Wang, D. B. Mitzi and Y. Yan, *J. Am. Chem. Soc.*, 2017, **139**, 6054–6057.